Journal of Manufacturing and Materials Processing

MDPI

Article

Effect of Laser Shock Peening on Gradient Microstructural Evolution and Mechanical Properties of Friction-Stir-Welded 7075 Aluminium Alloy Joints

Bin Hu [1] and Long Li [2,*]

[1] School of Mechanical and Automotive Engineering, Chuzhou Polytechnic, Chuzhou 239000, China; hubin@chzc.edu.cn
[2] College of Mechanical and Electrical Engineering, Nanjing University of Aeronautics and Astronautics, Nanjing 210016, China
* Correspondence: leelong@nuaa.edu.cn

Abstract

This study examines the effects of one-sided laser shock peening (LSP) on friction-stir-welded (FSW) 7075 aluminium alloy joints. It compares depth-dependent grain refinement, residual stress and local hardness in the nugget zone and relates these measurements to the transverse tensile response of the whole joint. Electron backscatter diffraction measurements at corresponding depths showed that the largest measured grain-size difference occurred 100 μm below the treated surface, where the mean grain size was 7.95 μm in the untreated joint and 1.54 μm after LSP. This difference diminished with depth. The weld-longitudinal residual stress changed from tensile to compressive at the treated surface, reaching approximately −280 MPa. It changed sign at a depth of 0.5–0.6 mm, while the treated and untreated stress profiles approached each other at approximately 0.9 mm. At a depth of 0.5 mm, microhardness increased from 126.8 to 135.6 HV. In transverse tension, mean yield strength increased from 346.8 to 383.9 MPa, ultimate tensile strength from 381.2 to 419.8 MPa, and elongation after fracture from 5.47% to 7.13%. These results show that LSP produced depth-dependent microstructural and residual stress changes, accompanied by local hardening and improvements in the tensile response of the joint.

Keywords: 7075 aluminium alloy; friction stir welding; laser shock peening; gradient microstructure; residual stress; mechanical properties

Academic Editor: Antonio Riveiro

Received: 7 October 2026
Revised: 9 November 2026
Accepted: 10 November 2026
Published: 12 November 2026

Copyright: © 2026 by the authors. Licensee MDPI, Basel, Switzerland. This article is an open access article distributed under the terms and conditions of the Creative Commons Attribution (CC BY) license.

1. Introduction

7075 aluminium alloy is a typical precipitation-strengthened, ultrahigh-strength Al–Zn–Mg–Cu alloy. Owing to its low density, high specific strength, excellent fatigue performance, and good damage tolerance, it is widely used in load-bearing aerospace structures, high-performance lightweight equipment, and precision structural components [1,2]. In aerospace service environments, critical load-bearing components often undergo complex cyclic loading, environmental corrosion, and coupled physical fields over extended periods. Consequently, welded joints must provide both high static load-bearing capacity and strong resistance to fatigue crack initiation and propagation to ensure long-term structural reliability [3]. As a heat-treatable, high-strength aluminium alloy, 7075 derives its superior mechanical properties primarily from finely dispersed η′/η ($MgZn_2$)

strengthening precipitates within the matrix. However, the high-temperature thermal cycles inherent in conventional fusion welding can dissolve precipitates and heterogeneous reprecipitation, and lead to grain coarsening, elemental segregation, porosity, and hot cracking, bringing about marked softening and degradation of welded-joint performance. Furthermore, residual tensile stresses arising from nonuniform heat input and cooling-induced contraction can further impair fatigue performance and shorten service life, substantially limiting the application of welded 7075 aluminium alloy in critical load-bearing structures [4,5].

Friction stir welding (FSW) is a well-established solid-state joining process that has been used to produce butt joints in AA7075-T651 aluminium alloy [6]. During FSW, frictional heating and plastic deformation soften the material around the rotating tool. As the tool advances, it drives the softened material around the pin to form a joint without bulk melting [7,8]. The coupled thermal and mechanical effects of FSW produce distinct microstructural changes across the nugget zone (NZ), the thermomechanically affected zone (TMAZ), and the heat-affected zone (HAZ). The NZ and TMAZ undergo both thermal cycling and plastic deformation, whereas the HAZ is primarily affected by thermal cycling, leading to pronounced microstructural heterogeneity across the joint [7]. In 7075 aluminium alloy, welding thermal cycles can induce the dissolution and coarsening of η′ strengthening precipitates and changes in their distribution. Together with welding-induced changes in grain structure, dislocation state, and residual stress distribution, these microstructural alterations influence the mechanical performance of the joint. Consequently, FSW joints generally exhibit lower strength than the base material [8]. Restoring and improving their overall mechanical performance therefore remains a critical issue for broadening the engineering application of FSW joints in high-strength aluminium alloys.

Current research aimed at mitigating the degradation of mechanical properties in FSW joints has primarily focused on three strategies, namely welding parameter optimisation, tool geometry design, and the application of auxiliary energy fields [9–11]. Optimising the tool rotation speed, welding speed, and pin geometry can improve material flow, promote dynamic recrystallisation, and refine grains in the NZ. However, the degradation of joint properties is closely associated with thermally induced precipitate evolution, changes in crystal defects, and the development of residual stresses. Adjusting welding parameters alone is therefore insufficient to fully eliminate joint softening, and further improvements in mechanical performance remain constrained by the underlying mechanisms of microstructural evolution [10].

In recent years, several assisted FSW techniques, including vibration-assisted FSW and forced-cooling-assisted FSW, have been investigated to regulate thermal conditions and material flow during welding [11]. Vibration-assisted FSW has been reported to refine the stir-zone grain structure in AA6061-T6 and AA5083 joints [12,13]. Grain refinement has also been observed in vibration-assisted friction stir spot welding of AA5083 [14]. Bagheri et al.[15] compared 6061-T6 aluminium alloy joints produced by FSW, friction stir vibration welding (FSVW), and tungsten inert gas (TIG) welding and found that FSVW improved joint strength, ductility, and impact toughness. Further studies have shown that combining vibration with water cooling can reduce heat accumulation in the weld region, suppress abnormal grain growth, and improve the mechanical performance of FSW joints in 5083 aluminium alloy [16]. Baradarani et al. [17] compared conventional and ultrasonic-assisted FSW of AZ91 magnesium alloy. They found that the stir zone of the ultrasonic-assisted weld had a higher fraction of high-angle grain boundaries and a stronger crystallographic texture, and attributed these changes to enhanced dynamic recovery and continuous dynamic recrystallisation during welding. Collectively, these investigations demonstrate opportunities for microstructural control during joint formation. Post-weld

treatment provides an additional route for tailoring the microstructure and residual stress state of an existing joint.

Post-weld heat treatment (PWHT) is another approach to improving the mechanical performance of precipitation-strengthened aluminium alloy FSW joints. Relevant treatments include direct artificial ageing and solution treatment followed by quenching and artificial ageing. Direct ageing can promote precipitation strengthening without an additional solution-treatment cycle, although its effectiveness depends on the heterogeneous solute and precipitate states remaining after welding [18]. Solution treatment followed by ageing can provide a more extensive modification of the precipitation state, but abnormal grain growth in the nugget zone may occur during high-temperature exposure, making the treatment response sensitive to the initial weld microstructure and thermal schedule [19]. Whereas post-weld ageing primarily modifies the precipitate distribution, laser shock peening (LSP) induces localised plastic deformation near the treated surface and can introduce compressive residual stresses. We therefore selected LSP to investigate how grain refinement and residual stress vary with depth in 7075 aluminium alloy FSW joints and how these changes relate to the tensile response of the joint as a whole.

Laser shock peening (LSP), an advanced surface strengthening technique based on plastic deformation, has attracted growing attention in recent years for improving the performance of aerospace metallic materials. Unlike conventional shot peening, LSP uses high-power-density laser pulses to generate rapidly expanding plasma beneath a confinement layer, producing high-amplitude shock pressure waves. These waves induce high-strain-rate plastic deformation in the near-surface region, introducing stable compressive residual stresses to substantial depths. Meanwhile, the high-rate shock loading promotes dislocation multiplication and entanglement, subgrain formation, and grain refinement, producing a heterogeneous microstructure with a depth-dependent gradient. These effects contribute to simultaneous improvements in tensile strength, fatigue performance, and resistance to cracking [20,21].

Numerous studies in recent years have demonstrated that LSP can improve the service performance of metallic materials through the combined effects of residual stress modification and microstructural strengthening. Pan et al. [22] investigated LSP-treated 7075 aluminium alloy and found that the high-density dislocation structures and gradient grain structures induced by laser shock loading significantly increased the fatigue limit. LSP also promoted the formation of nanoscale precipitates, which inproved microstructural stability under cyclic loading. Their study further highlighted the combined contribution of dynamic precipitation and compressive residual stresses to the improved fatigue performance of 7075 aluminium alloy. In addition to introducing compressive residual stresses, LSP can promote grain refinement and the evolution of crystal defects in high-strength aluminium alloys. Dhakal and Swaroop [23] reported that LSP treatment of 7075 aluminium alloy produced a distinct work-hardened surface layer, significantly reduced the grain size, and increased the fraction of low-angle grain boundaries. These observations indicated that shock-induced plastic deformation promoted dislocation rearrangement and subgrain formation. Furthermore, He et al. [24] investigated the effects of laser shock peening parameters on the residual stresses and mechanical properties of aluminium alloys. They found that the number of peening passes and laser energy density significantly influenced the magnitude of compressive residual stresses, and that appropriate parameter optimisation could produce a more stable residual stress gradient.

LSP has also been widely applied to welded structures to improve the residual stress state and fatigue performance of joints in various materials. In 7075 aluminium alloy, the compressive residual stresses introduced by LSP depend on both laser pulse energy and spot overlap [25]. The relevance of these stresses to fatigue performance has been demon-

strated in corrosion-exposed 7075-T651 specimens, where LSP extended fatigue life relative to the untreated, corroded condition. The authors attributed this improvement to compressive residual stresses counteracting the local tensile stresses around corrosion pits [26]. For Monel 400, Palmeh et al. [27] showed that micro-shot peening coverage affected surface integrity and corrosion resistance. Treatment at 1500% coverage improved resistance to corrosion in hydrofluoric acid, whereas increasing the coverage to 2000% produced surface microcracks and reduced corrosion resistance relative to the 1500% condition.

In recent years, LSP has been investigated as a post-weld treatment for improving the microstructure and mechanical properties of aluminium alloy FSW joints. Dhanasekaran et al. [28] reported that LSP changed tensile residual stresses to compressive stresses and increased the surface and subsurface hardness of an AA2219 joint. Using finite element simulations, Li et al. [29] found that increasing laser power density enhanced plastic deformation and extended the region affected by compressive residual stresses, although the residual stress response approached saturation at higher energy inputs. Dai et al. [30] showed that LSP improved the uniformity of local microstructure and mechanical properties in an Al–Cu joint, accompanied by increases in strength and elongation. For an AA6061-T6 joint, Wu et al. [31] combined microstructural characterisation, depth-resolved residual stress measurements and tensile testing to examine the effects of LSP. More recently, Dhanasekaran et al. [32] used electron backscatter diffraction, transmission electron microscopy and X-ray diffraction to investigate the microstructural response of an AA2219 weld to different LSP treatments. These studies demonstrate that LSP can modify the stress state and mechanical behaviour of aluminium alloy welds. The alloy composition and initial weld microstructure should be considered when interpreting the response of a 7075 joint.

For friction-stir-welded 7075 aluminium alloy joints, previous studies have also examined the effects of laser peening. Hatamleh et al. [33] investigated fatigue crack growth in 7075-T7351 joints and reported a reduction in crack growth rate after laser peening. Hatamleh and DeWald [34] measured residual stress distributions in peened 7075-T651 joints. These studies provide a basis for evaluating the fatigue behaviour and residual stress state of laser-peened 7075 welds.

A remaining question is how the variation in grain refinement with depth in the nugget zone relates to the depth-dependent residual stress distribution after LSP. Examining these changes alongside local hardness and the tensile response can help interpret how a surface treatment affects a heterogeneous welded joint. Accordingly, the present study compares untreated and one-sided LSP-treated friction-stir-welded 7075 aluminium alloy joints. Electron backscatter diffraction, X-ray diffraction, microhardness measurements, depth-resolved residual stress analysis and transverse tensile testing are used to characterise the treated and untreated conditions. The contribution of this study is to compare depth-dependent grain refinement and residual stress redistribution in the nugget zone with local hardness and the transverse tensile response of the same welded joint condition.

2. Materials and Methods

7075 aluminium alloy was used in this study. Rectangular specimens measuring 100 mm × 50 mm × 4 mm (length × width × thickness) were prepared by conventional machining, with the longitudinal direction aligned with the rolling direction. The chemical composition is listed in Table 1.

Table 1. Chemical composition of 7075 aluminium alloy (%, mass fraction).

Zn	Mg	Cu	Mn	Ti	Cr	Fe	Si	Al
5.1~6.1	2.1~2.9	1.2~2.0	0.3	0.072	0.18–0.28	0.5	0.4	bal

Figure 1 summarises the fabrication, laser shock peening (LSP), specimen extraction, and characterisation procedures for the 7075 aluminium alloy friction-stir-welded joints. Figure 1a illustrates the FSW and subsequent LSP processes, together with the welding tool geometry. Before welding, the surface oxide film was removed from the aluminium plates, and the mating surfaces were cleaned with anhydrous ethanol. FSW was performed using an FSW-3LM-003M welding machine (Beijing FSW Technology Co., Ltd., Beijing, China) and an H13 hot-work tool steel tool. The tool rotation speed, welding speed, and tilt angle were 1000 rev min^{-1}, 60 mm min^{-1}, and 2°, respectively. The tool comprised a clamping shank of Φ20 h6, a grooved body with an outer diameter of 28 mm, and a working shoulder with a diameter of 12 mm. The conical pin protruded 4 mm from the shoulder face and had root and tip diameters of 5 and 4 mm, respectively.

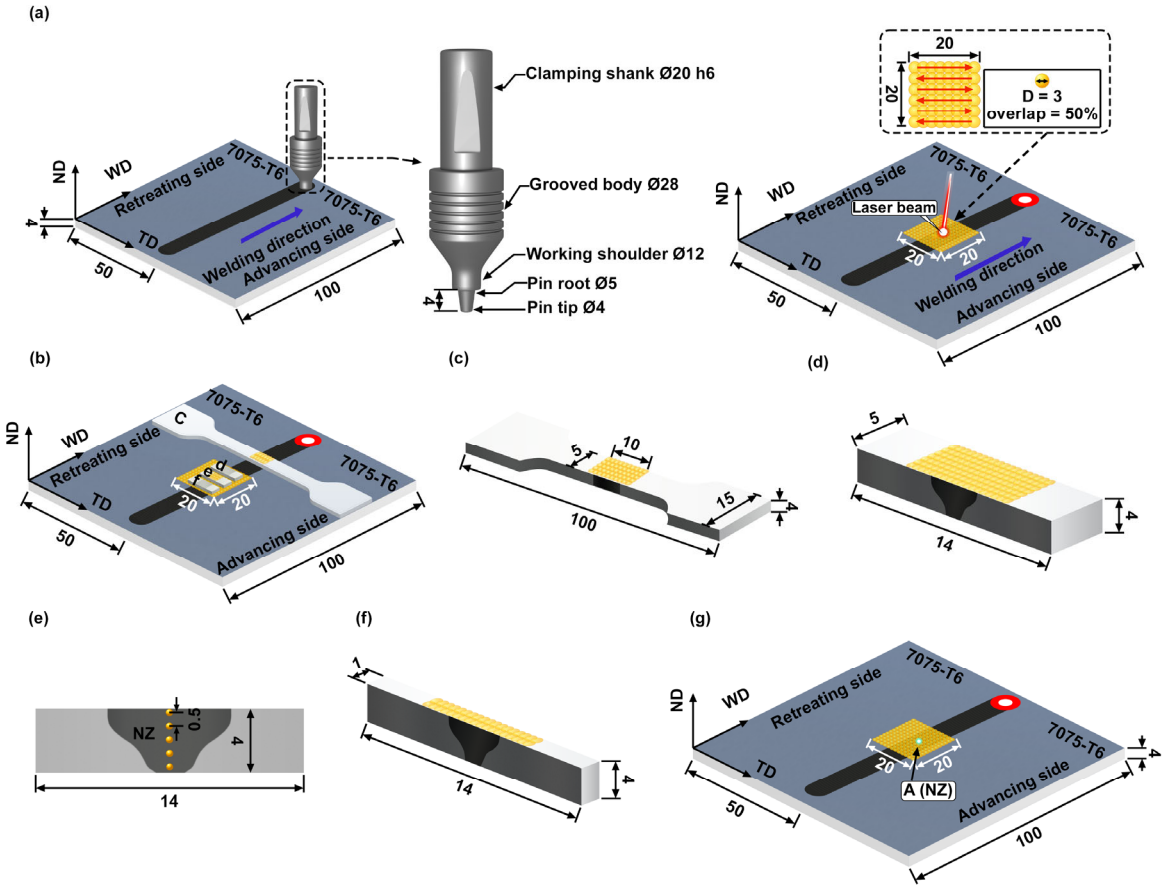


Figure 1. Schematic illustrations of the fabrication, laser shock peening (LSP), specimen extraction, and measurement arrangements for 7075 aluminium alloy friction-stir-welded (FSW) joints. (**a**) FSW process, welding tool geometry, and LSP treatment area and scanning pattern; (**b**) specimen extraction layout; (**c**) tensile specimen geometry and dimensions; (**d**) electron backscatter diffraction (EBSD) specimen; (**e**) microhardness measurement positions in the nugget zone (NZ); (**f**) specimen for X-ray diffraction phase analysis; (**g**) location of point A in the NZ for depth-resolved residual stress measurements. the schematic, ND, WD, and TD denote the normal, welding, and transverse directions, respectively. NZ denotes the nugget zone. The arrows indicate the welding direction, and the dimensions are given in millimeters unless otherwise specified. The yellow area indicates

the laser shock peening (LSP) treatment region. All dimensions are in mm unless otherwise indicated.

After welding, LSP was performed using a YS1505-R200A system manufactured by Xi'an Tianruida, China. The laser pulse energy, pulse duration, and wavelength were 15 J, 20 ns, and 1064 nm, respectively. A circular spot with a diameter of 3 mm was used, with a 50% overlap between adjacent spots. A 0.1-mm-thick black adhesive tape served as the ablative layer, and a 1–2-mm-thick flowing water film served as the confinement layer. As illustrated in Figure 1a, the 20 mm × 20 mm treatment region was centred on the weld and extended into the adjacent material on both sides. A serpentine scanning pattern was adopted, with alternating scans perpendicular to the weld and successive row increments along the welding direction. The treatment region was scanned twice, and the black adhesive tape was replaced between passes.

Figure 1b shows the specimen extraction layout. All characterisation and mechanical tests were conducted under identical conditions for the as-welded FSW and LSP-treated FSW (FSW + LSP) joints. Tensile specimens were extracted perpendicular to the welding direction using wire electrical discharge machining in accordance with ISO 6892-1:2019.

As shown in Figure 1c, the specimens had an overall length of 100 mm, a grip width of 15 mm, a reduced-section width of 5 mm, and a thickness of 4 mm. The central treated segment indicated in the figure was 10 mm long. Room-temperature tensile tests were performed in accordance with ISO 6892-1:2016 using a computer-controlled electronic universal testing machine (GNT series,NCS Testing Technology Co., Ltd., Beijing, China) at a constant crosshead speed of 1 mm min^{-1}. Engineering strain was measured using an extensometer with a gauge length of 25 mm. The yield strength was determined as the 0.2% proof stress, Rp0.2, using a line parallel to the initial linear elastic portion of the engineering stress–strain curve and offset by a strain of 0.002. Three replicate tests were conducted for each joint condition. After testing, the fracture surfaces were cleaned and examined by scanning electron microscopy to characterise their morphology.

Electron backscatter diffraction (EBSD) was used to characterise the joint microstructure. The specimen geometry is shown in Figure 1d, with dimensions of 14 mm × 5 mm × 4 mm. The specimens were ground using 4000-grit abrasive paper and polished with a colloidal alumina suspension containing 50 nm particles. Electropolishing was subsequently performed in an ethanol–perchloric acid electrolyte with a volume ratio of 4:1 at 0 °C and 20 V. EBSD measurements were conducted using a JSM-7900F field-emission scanning electron microscope (JEOL Ltd., Akishima, Tokyo, Japan) equipped with a DigiView V EBSD detector (EDAX Inc., Mahwah, NJ, USA), at an accelerating voltage of 15 kV and a step size of 0.2 μm. The data were analysed using OIM Analysis 9 software, and spurious indexed points and non-indexed points were removed during data cleaning.

Figure 1e illustrates the microhardness measurement positions within the nugget zone (NZ). Vickers microhardness measurements were performed on the joint cross-sections using a Fness V2000CA microhardness tester (FEMA Automation Technology Co., Ltd., Suzhou, China) under a load of 300 g and a dwell time of 15 s. The measurement points were arranged along the thickness direction within the NZ, with a spacing of 0.5 mm between adjacent indentations. This arrangement was selected to characterise the through-thickness hardness distribution and to compare the untreated and LSP-treated joints at corresponding depths. The resulting profiles were used to assess local hardening beneath the treated surface and its variation with depth. At least three replicate measurements were performed for each joint condition.

The specimens shown in Figure 1f, with dimensions of 14 mm × 1 mm × 4 mm, were used for X-ray diffraction phase analysis. Measurements were performed using a Philips X'Pert diffractometer with Cu Kα radiation at a tube voltage of 42 kV and a tube current

of 40 mA. Continuous scanning was conducted over a 2θ range of 3.01–79.96° at a scan rate of 6° min^{-1}.

As shown in Figure 1g, depth-resolved residual stresses were measured at point A within the NZ of both the FSW and FSW + LSP joints using an EDGE portable residual stress analyser manufactured by GNR, Agrate Conturbia, Italy. The in-plane residual stress component parallel to the welding direction was determined using the Al {311} diffraction reflection and the X-ray diffraction iso-inclination method. The diffraction angle, 2θ, was 140.01°, the tube voltage was 33 kV, the tube current was 0.08 mA, and the collimator diameter was 2 mm. Depth profiles were obtained by successive electropolishing, with approximately 100 μm of material removed at each step. Residual stresses were measured on the newly exposed surface after each removal step. The specimen thickness was measured before and after each step using a digital micrometer with a resolution of 1 μm. The cumulative depth relative to the original surface was calculated by summing the measured thickness reductions.

3. Results

3.1. Microstructure

Figure 2 shows the cross-sectional macrostructures of the joints. Both the FSW and FSW + LSP joints retain their characteristic weld morphology, with a typical onion-ring structure in the nugget zone (NZ). Both joints exhibit sound weld formation, with no visible macroscopic defects, such as pores or cracks. Compared with the as-welded FSW joint, the FSW + LSP joint exhibits local plastic deformation in the NZ induced by shock loading, accompanied by changes in the bottom contour of the NZ and an apparent extension of the pre-existing material flow patterns. Three observation regions, designated S1, S2, and S3 and marked by red boxes, were selected along the thickness direction of the NZ to further examine the through-thickness variations associated with thermomechanical coupling during joint formation.

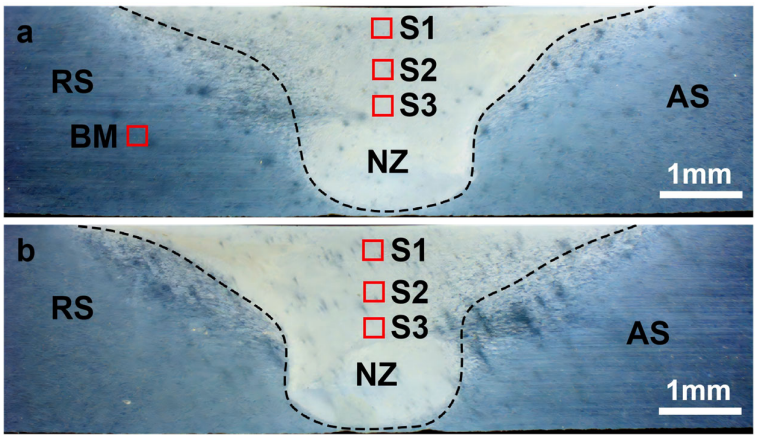


Figure 2. Optical micrographs of joint cross-sections (**a**) FSW joint; (**b**) FSW + LSP joint.

Figure 3 presents the EBSD characterisation results for the base metal (BM). The inverse pole figure (IPF) map in Figure 3a reveals distinctly elongated grains extending along the rolling direction, with a broad grain size distribution characteristic of a rolled microstructure. The different colours represent variations in crystallographic orientation among the grains. The average grain size of the BM was determined to be 36.1 μm.

Figure 3b shows the kernel average misorientation (KAM) map of the base metal, with an average KAM value of 1.03°. Most regions exhibit relatively low local misorientation, while isolated regions of higher KAM are observed near some grain boundaries. The

elongated grain morphology is consistent with deformation along the rolling direction during prior processing. Differences in deformation and lattice rotation between neighbouring grains may have produced local orientation gradients near their boundaries. These observations are consistent with heterogeneous deformation associated with the processing history of the base metal.

Figure 3c presents the recrystallisation classification map. Recrystallised, substructured, and deformed grains account for 73.5%, 24.4%, and 2.1%, respectively. These results indicate that the BM microstructure is predominantly composed of recrystallised grains, while retaining a smaller fraction of rolling-induced substructures and very few deformed grains.

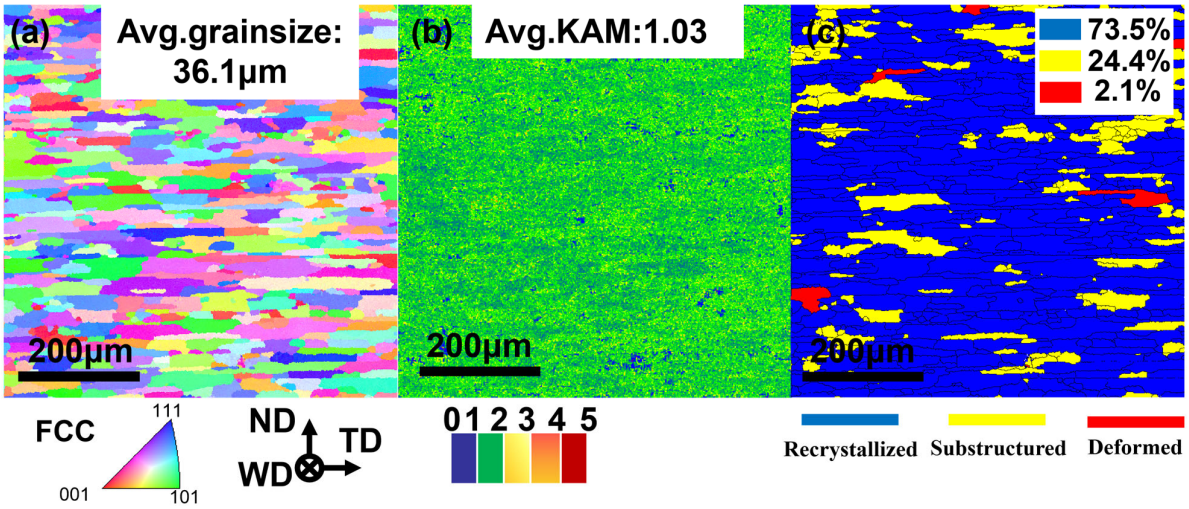


Figure 3. EBSD characterization of the base metal (BM): (**a**) inverse pole figure (IPF) map; (**b**) kernel average misorientation (KAM) map; (**c**) recrystallisation classification map.

Figure 4 shows inverse pole figure (IPF) maps of the nugget zone in the FSW and FSW + LSP joints. In the untreated FSW joint, the mean grain sizes measured in regions S1, S2 and S3 were 7.95, 8.16 and 8.19 μm, respectively (Figure 4a–c). The difference between the largest and smallest regional means was 0.24 μm. Thus, the three regions sampled in the untreated joint had similar mean grain sizes.

In contrast, the NZ exhibits pronounced gradient grain refinement after LSP treatment, as shown in Figure 4d–f. The average grain size in S1 decreases to 1.54 μm, indicating substantial grain refinement. With increasing depth from the LSP-treated surface, the average grain size increases to 5.39 μm in S2 and further to 8.09 μm in S3, approaching that of the untreated FSW joint. The reduction in mean grain size near the treated surface is consistent with severe plastic deformation induced by the LSP shock wave. Dislocation accumulation and rearrangement may promote the formation of subgrain structures, while further deformation may increase misorientation across some subgrain boundaries and contribute to grain subdivision. The post-treatment EBSD observations demonstrate grain refinement, although they do not directly resolve the sequence of these processes during shock loading. As the shock wave propagates into the material, its attenuation reduces the extent of plastic deformation, progressively weakening the grain refinement effect. Consequently, the FSW + LSP joint develops a through-thickness gradient microstructure, transitioning from an ultrafine-grained near-surface region to a deeper region largely unaffected by the treatment.

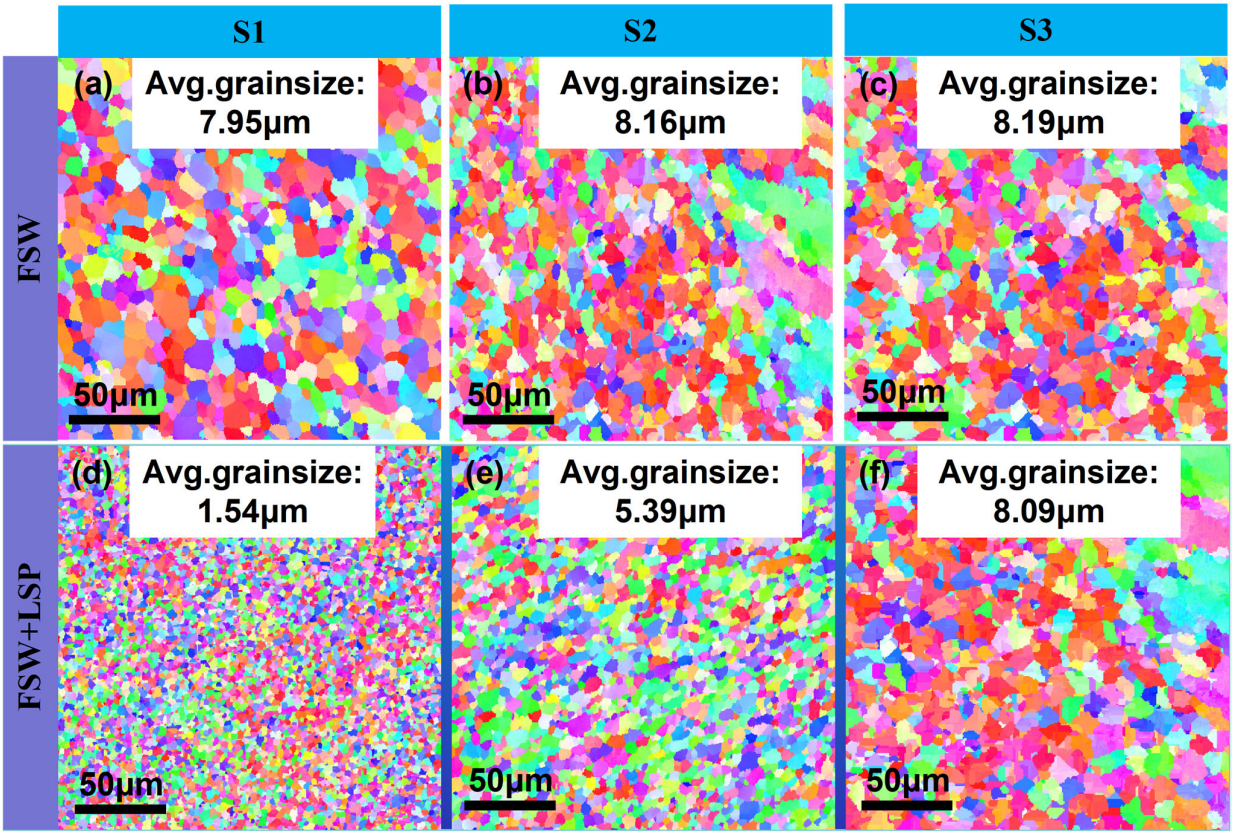


Figure 4. Inverse pole figure maps of the nugget zone at three sampling depths in the 7075 aluminium alloy joints. Panels (**a**–**c**) show regions S1, S2 and S3 in the untreated FSW joint, respectively. Panels (**d**–**f**) show the corresponding regions in the FSW + LSP joint. The centre depths of S1, S2 and S3, measured from the top surface of the weld, were 100, 500 and 900 μm, respectively. The colours represent the crystallographic orientations of the grains, as indicated by the inverse pole figure (IPF) colour key.

Figure 5 presents the recrystallisation classification maps at different depths in the NZ of the FSW and FSW + LSP joints. As shown in Figure 5a–c, the recrystallised grain fractions in regions S1, S2, and S3 of the FSW joint are 80.9%, 79.0%, and 80.3%, respectively. These fractions show little variation with depth and are consistently higher than that of the BM (73.5%). These observations are consistent with microstructural restoration and grain refinement during FSW. As material flows around the rotating tool, intense shear deformation promotes dislocation multiplication and the accumulation of stored deformation energy. The accompanying temperature rise can facilitate dislocation rearrangement and annihilation, leading to dynamic recovery and the formation of subgrain structures. With continued deformation, the misorientation between some neighbouring subgrains may increase, allowing low-angle boundaries to evolve into high-angle boundaries and contributing to the formation of fine grains through continuous dynamic recrystallisation. This mechanism provides a possible explanation for the refined NZ microstructure. However, the post-weld EBSD maps describe the final microstructure and do not directly establish the sequence or relative contribution of the restoration mechanisms during welding.

Following LSP treatment, the recrystallised grain fractions in S1, S2, and S3 are 85.2%, 82.6%, and 80.1%, respectively, as shown in Figure 5d–f. Compared with the corresponding regions of the FSW joint, the fractions increase in S1 and S2, whereas S3 remains essentially unchanged. This depth-dependent response suggests that LSP-induced high-

strain-rate plastic deformation is concentrated primarily in the near-surface region. The associated dislocation accumulation, subgrain formation, and grain boundary evolution may facilitate the formation of high-angle grain boundaries, contributing to the increased fraction of grains classified as recrystallised. As the distance from the treated surface increases, attenuation of the laser-induced shock wave progressively reduces its influence on plastic deformation and microstructural evolution. Consequently, the deeper region (S3) largely retains the original microstructural characteristics of the FSW joint.

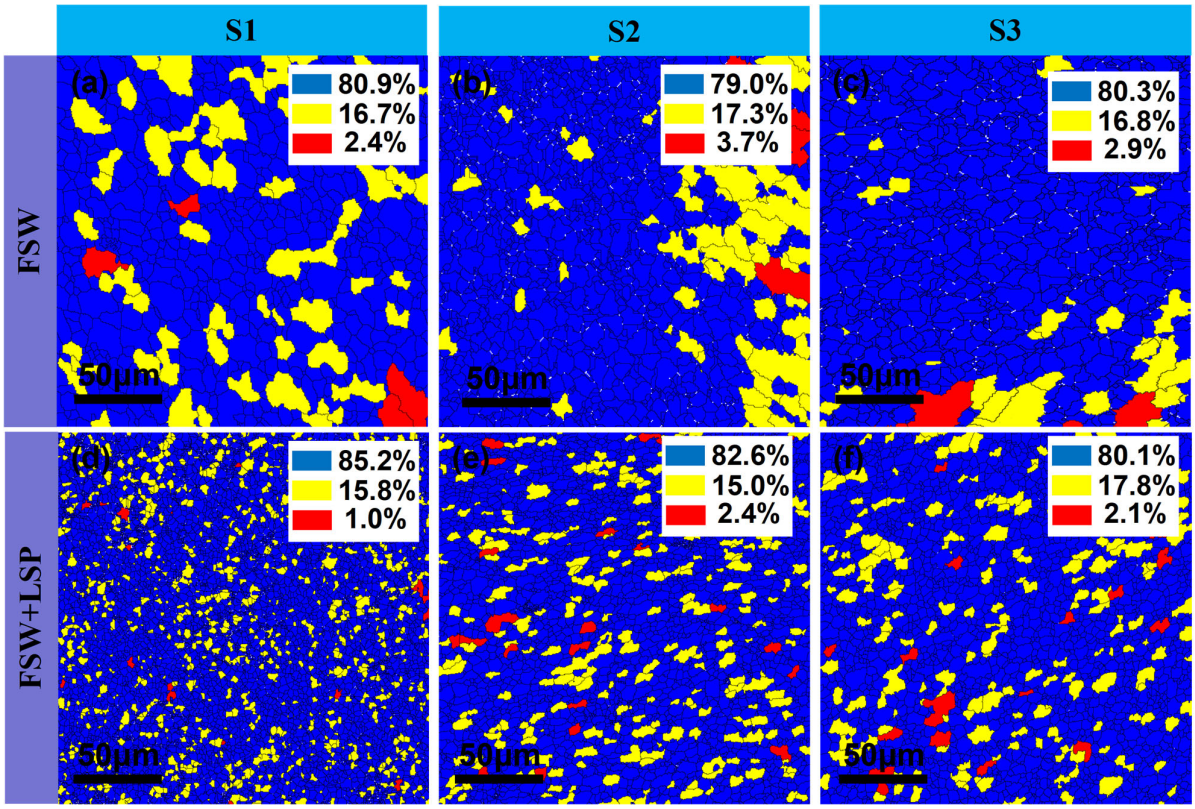


Figure 5. GOS maps of the nugget zone (NZ) in FSW and FSW + LSP joints. (**a–c**) S1–S3 of the nugget zone for the FSW joint; (**d–f**) S1–S3 of the nugget zone for the FSW + LSP joint.

Figure 6 presents the kernel average misorientation (KAM) maps of the NZ. As shown in Figure 6a–c, the average KAM values in regions S1, S2, and S3 of the FSW joint are 0.63°, 0.78°, and 0.80°, respectively. The lower average KAM value in S1 may reflect differences in the thermomechanical conditions experienced by the material at different depths. In addition to temperature, the local strain, strain rate, material flow and duration of thermal exposure can influence dislocation accumulation and restoration during FSW. Variations in these factors may therefore contribute to the higher local misorientation measured in S2 and S3. Because the local temperature and deformation histories were not measured, the relative contribution of each factor cannot be determined from the present KAM maps. All three regions also exhibit lower average KAM values than the base metal (1.03°), indicating lower local misorientation at the EBSD measurement scale.

Following LSP treatment, the average KAM values in S1, S2, and S3 are 0.38°, 0.68°, and 0.81°, respectively, as shown in Figure 6d–f. Region S1 exhibits the lowest average KAM value. Although LSP-induced high-strain-rate plastic deformation initially introduces dislocations and lattice distortion, subsequent dislocation rearrangement and possible recovery processes may reduce intragranular orientation gradients, contributing to

the lower KAM value. At greater depth, in region S2, attenuation of the shock wave reduces the extent of plastic deformation and the associated microstructural evolution, and the average KAM value increases to 0.68°. In region S3, the average KAM value is essentially unchanged from that of the corresponding region in the FSW joint (0.80°), suggesting that the influence of LSP on local misorientation is negligible at this depth. These results indicate that LSP primarily modifies near-surface lattice distortion, with little measurable effect on the deeper region of the NZ.

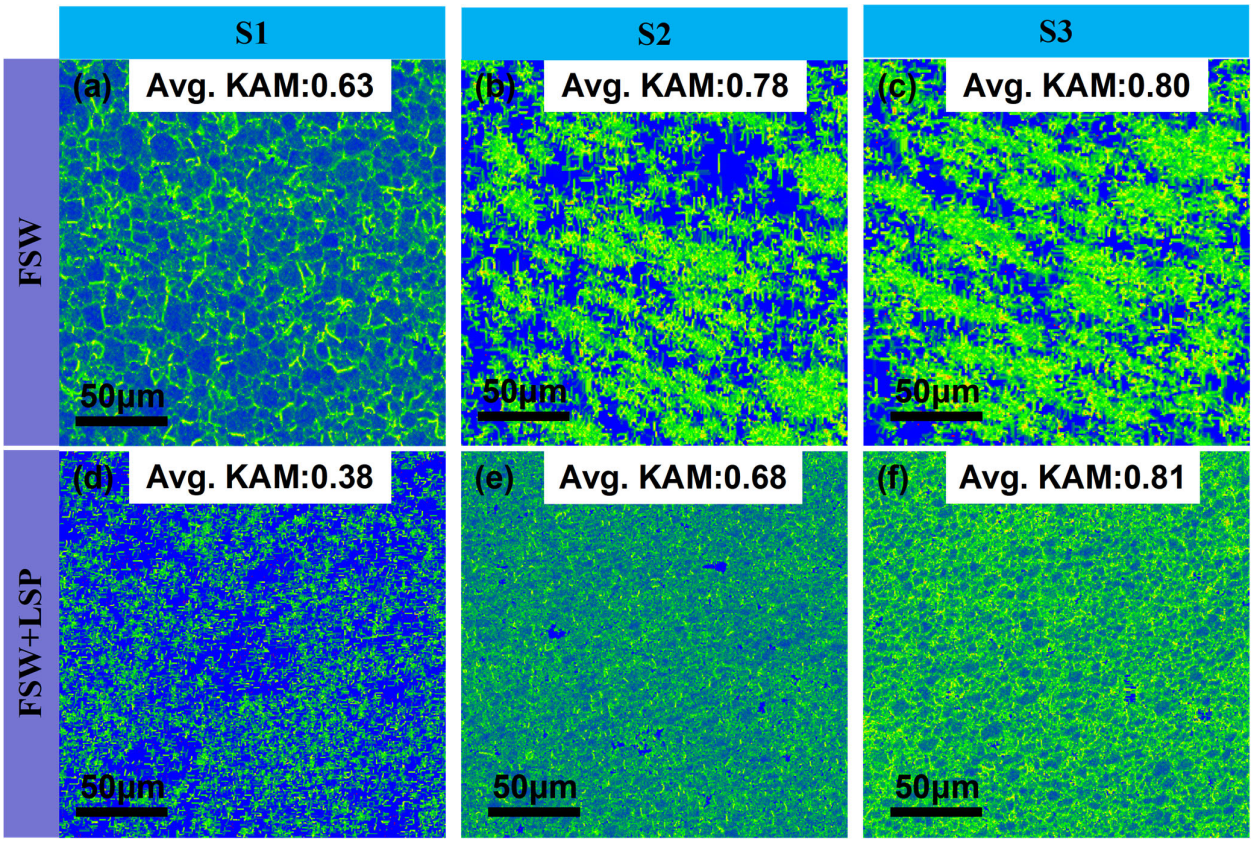


Figure 6. KAM maps of the nugget zone (NZ) in FSW and FSW + LSP joints. (**a–c**) S1–S3 of the nugget zone for the FSW joint; (**d–f**) S1–S3 of the nugget zone for the FSW + LSP joint. The colours represent the distribution of kernel average misorientation (KAM); higher KAM values are indicated by green, and lower values by blue, as shown in the KAM colour scale.

3.2. XRD Analysis

Figure 7 presents the XRD patterns obtained from the cross-sections of the FSW and FSW + LSP joints. Both joints exhibit similar diffraction features, with distinct peaks at 2θ values of 38.5°, 44.7°, 65.1°, and 78.2°, corresponding to the (111), (200), (220), and (311) planes of the face-centred cubic (FCC) α-Al matrix, respectively. These peaks agree with the standard diffraction data (PDF No. 04-003-7125), indicating that the α-Al solid solution remains the predominant phase in both joints, with no detectable change in phase constitution following LSP treatment.

Comparison of the two XRD patterns shows that the α-Al peak positions remain essentially unchanged after LSP, and no additional diffraction peaks are detected. The principal α-Al peaks in the FSW + LSP pattern appear broader and exhibit lower peak heights than those in the FSW pattern. Peak broadening may be associated with changes in coherent diffraction domain size and microstrain arising from lattice defects. The measured peak profiles also include an instrumental contribution. In addition, the recorded peak

heights may be affected by peak broadening, crystallographic texture, specimen surface condition and measurement geometry. No instrumental broadening correction or quantitative peak-profile analysis was performed; therefore, the relative contributions of these factors cannot be determined from the present patterns.

No distinct diffraction peaks associated with the principal strengthening precipitates in 7075 aluminium alloy are observed. This may be attributed to their low volume fraction, small size, and partial dissolution during the FSW thermal cycle, resulting in diffraction signals below the detection limit of XRD. Overall, these results suggest that LSP improves joint performance primarily through dislocation strengthening, grain refinement, and the introduction of compressive residual stresses, without detectable changes in phase constitution.

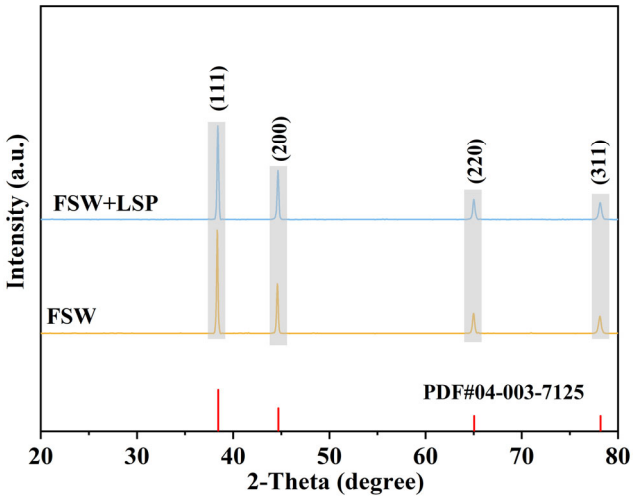


Figure 7. XRD patterns of cross-sections of FSW and FSW + LSP joints.

3.3. Residual Stress Analysis

Figure 8 presents the residual stress measurement procedure and the through-thickness residual stress distributions of the FSW and FSW + LSP joints. Figure 8a–c show the experimental setup and measurement procedure using X-ray diffraction, while Figure 8d shows the residual stress profiles as a function of depth.

As shown in Figure 8d, the FSW joint exhibits tensile residual stresses throughout the investigated depth range of 0–2000 μm. The surface residual stress is 139.8 MPa and generally decreases with increasing depth, reaching 79.5 MPa at the plate mid-thickness (2000 μm). This distribution is likely associated with the nonuniform thermal cycles, plastic deformation, and constrained cooling contraction during FSW. During cooling, contraction of the weld region is constrained by the surrounding material, resulting in tensile residual stresses. Variations in thermal history, plastic deformation, and constraint conditions through the plate thickness further contribute to the nonuniform residual stress distribution.

Following LSP, the longitudinal residual stress at the treated surface was approximately −280 MPa, compared with a tensile stress of 139.8 MPa at the corresponding surface of the untreated FSW joint (Figure 8d). In the treated joint, the longitudinal residual stress changed from compressive to tensile at a depth of 0.5–0.6 mm. At approximately 0.9 mm below the surface, the longitudinal residual stress in the treated joint approached that in the untreated joint. This behavior is consistent with plastic deformation induced in the near-surface region by laser-generated shock waves, followed by the development of compressive residual stresses under the constraint of the surrounding and underlying

material upon unloading. As the shock waves propagate into the material and attenuate, the induced plastic deformation becomes less pronounced, leading to a gradual decrease in the magnitude of the compressive residual stress.

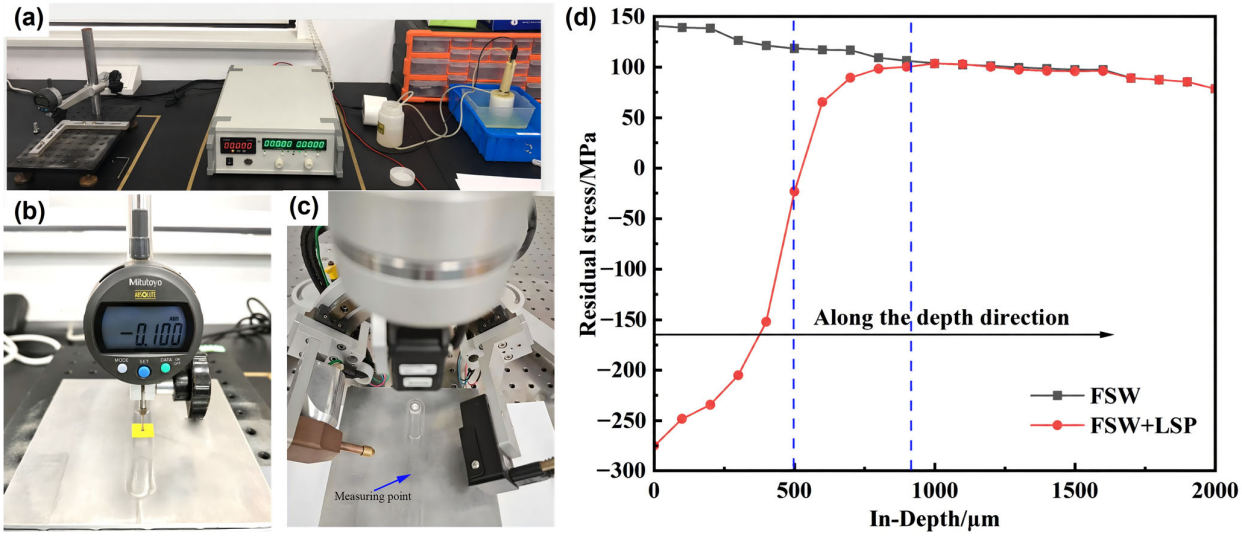


Figure 8. Residual stress testing setup and residual stress distribution along depth direction. (**a**) Special experimental platform for residual stress measurement; (**b**) calibration device with high-precision dial indicator; (**c**) schematic diagram of fixed-point residual stress detection; (**d**) residual stress distribution along depth of FSW and FSW + LSP joints.

3.4. Microhardness Analysis

Figure 9 presents the depth-dependent microhardness profiles in the NZ of the FSW and FSW + LSP joints. Both joints exhibit an initial decrease followed by an increase in microhardness with increasing distance from the weld surface, resulting in an overall U-shaped distribution. In the untreated FSW joint, the measured microhardness was approximately 129.8 HV near the top surface and decreased to approximately 110.8 HV at a depth of 2 mm, before increasing to approximately 125.2 HV at 4 mm. Thus, the near-surface value was higher than the measured value near the mid-thickness of the same joint. Through-thickness differences in the thermal and deformation histories during FSW may have affected the local strengthening precipitates and defect structure, contributing to the observed hardness distribution. The mean grain sizes measured in the three NZ regions were similar, ranging from 7.95 to 8.19 μm. The available results do not establish which microstructural factor was primarily responsible for the hardness difference.

At a depth of 0.5 mm below the top surface, the NZ microhardness was 126.8 HV in the untreated FSW joint and 135.6 HV in the FSW + LSP joint (Figure 9), an increase of approximately 6.9% following LSP. This comparison shows local hardening at the measured depth. The depth dependence of grain refinement was assessed separately using the EBSD measurements reported in Section 3.1.

The microhardness enhancement gradually diminishes with increasing depth from the treated surface. Within the depth range of 1–2 mm, the profiles of the FSW + LSP and FSW joints progressively converge, indicating that shock wave attenuation limits the extent of induced plastic deformation and microstructural strengthening. At depths of 3–4 mm, the two joints exhibit essentially identical microhardness values, suggesting that LSP has little measurable influence in this region, where hardness is governed primarily by the FSW thermal cycle and the pre-existing microstructure.

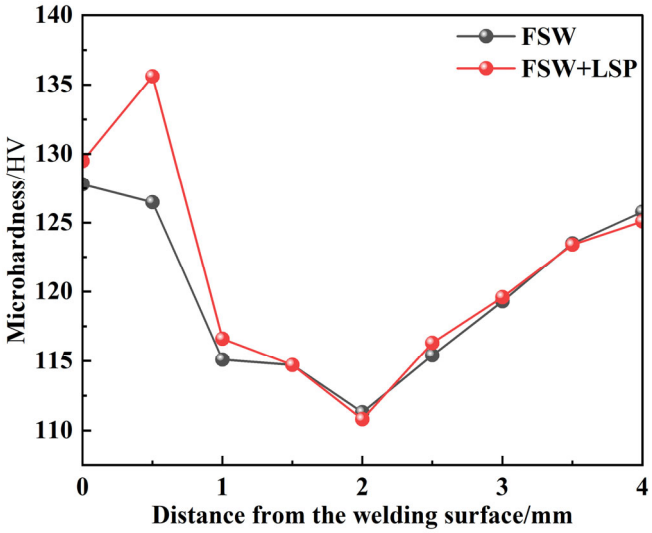


Figure 9. Microhardness along the depth direction of the nugget zone.

3.5. Tensile Properties and Fracture Analysis

Figure 10 presents the tensile test results for the FSW and FSW + LSP joints. As shown in Figure 10a, both joints exhibit similar linear stress–strain responses during elastic deformation, suggesting that LSP treatment has little influence on their elastic behaviour and elastic modulus. However, their stress–strain curves progressively diverge upon yielding and subsequent plastic deformation. After yielding, the FSW + LSP joint exhibited higher engineering stress than the untreated FSW joint over the strain range common to both curves (Figure 10a). Elongation after fracture increased from 5.47% to 7.13% (Figure 10b), a gain of 1.66 percentage points, or approximately 30% relative to the untreated joint. The results summarised in Figure 10b further demonstrate the beneficial effects of LSP on the mechanical properties of the FSW joints. For the untreated FSW joints, the yield strength (YS), ultimate tensile strength (UTS), and elongation after fracture (FE) were 346.8 ± 4.82 MPa, 381.2 ± 4.30 MPa, and 5.47 ± 0.23%, respectively. Following LSP treatment, these values increase to 383.9± 5.40 MPa, 419.8± 5.14 MPa, and 7.13± 0.27%, corresponding to improvements of 10.69%, 10.12%, and 30.34%, respectively. These results indicate that LSP enhances both the load-bearing capacity and plastic deformation capability of the joints, achieving simultaneous improvements in strength and ductility.

The improved tensile properties of the FSW + LSP joints were accompanied by near-surface grain refinement and local hardening. These changes may have increased resistance to plastic deformation in the treated region. During transverse tensile loading, the treated surface layer and the underlying material deform together and contribute to the measured response of the joint. LSP also modified the residual stress distribution; however, the measured stress component was parallel to the weld, whereas the tensile load was applied perpendicular to the weld. The relative contributions of grain refinement, other microstructural changes and residual stress to the measured tensile properties cannot be determined from the present results.

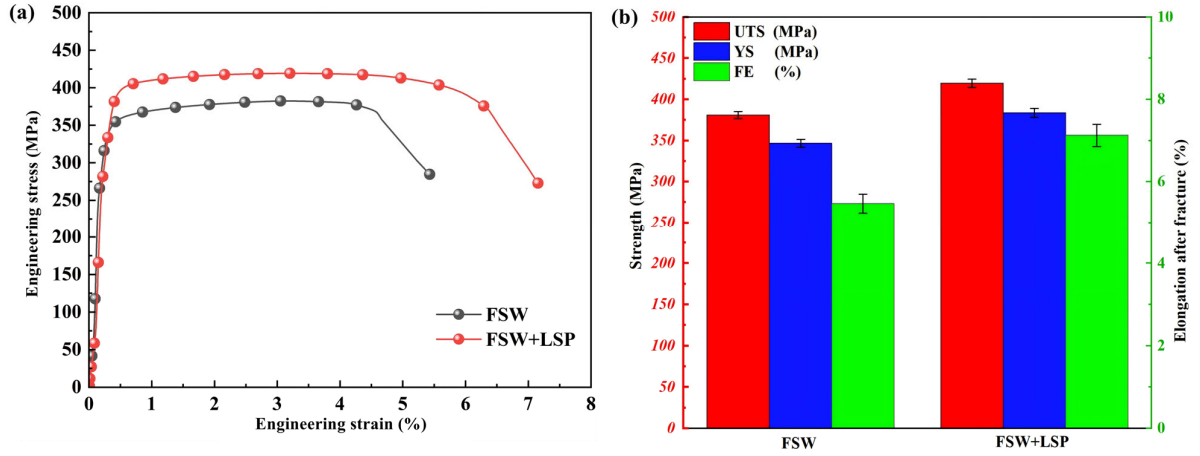


Figure 10. Tensile properties of the FSW and FSW + LSP joints: (**a**) representative engineering stress–strain curves; (**b**) ultimate tensile strength (UTS), yield strength (YS), and elongation after fracture (FE). Bars show the mean of three specimens per condition, and error bars indicate ±1 standard deviation.

Figure 11 shows the macroscopic appearance of representative FSW and FSW + LSP tensile specimens after testing. The enlarged views show the regions around the fracture locations. Both specimens fractured in the nugget zone (NZ). The fracture surfaces were subsequently examined by scanning electron microscopy to compare their microscopic morphologies.

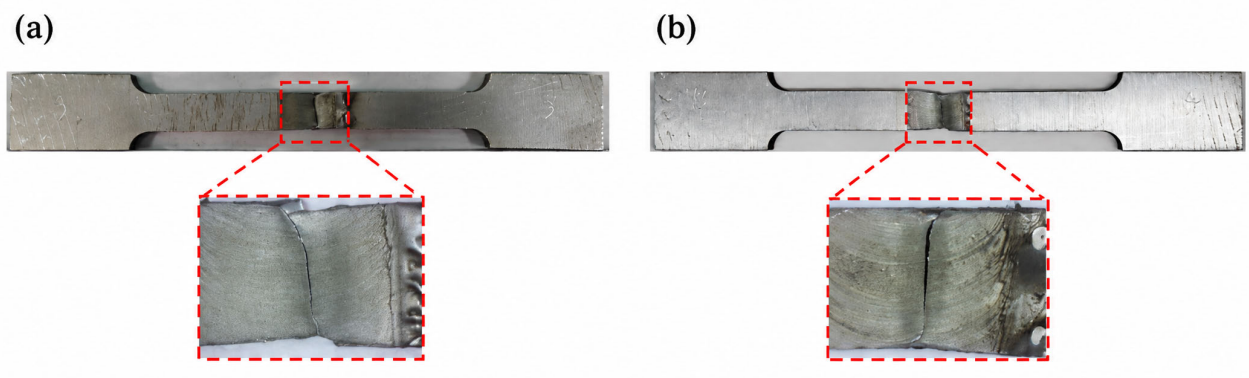


Figure 11. Macroscopic appearance of representative tensile specimens after testing: (**a**) FSW joint and (**b**) FSW + LSP joint. The enlarged views show the regions around the fracture locations.

To further elucidate the effects of LSP on the tensile deformation behaviour and fracture mechanisms of the FSW joints, the tensile fracture surfaces were examined using scanning electron microscopy (SEM), as shown in Figure 12.

As shown in Figure 12a–c, the untreated FSW joint exhibits predominantly ductile fracture features, although the extent of plastic deformation is relatively limited. At low magnification (Figure 12a), numerous fine dimples are visible on the fracture surface, with a non-uniform distribution and local regions exhibiting quasi-cleavage features. Higher-magnification observations (Figure 12b,c) reveal small, shallow dimples, some of which are incompletely developed, together with a few regions showing tearing features. These observations suggest relatively limited microvoid growth and coalescence during tensile deformation, consistent with the lower elongation after fracture of the FSW joint (5.47%).

In contrast, the FSW + LSP joint exhibits more pronounced ductile fracture characteristics. As shown in Figure 12d–f, the fracture surface appears more uniform at low magnification, without extensive flat fracture regions. Higher-magnification images reveal numerous larger and deeper equiaxed dimples with well-defined edges and prominent tear ridges, indicating more extensive plastic deformation before fracture. The larger, deeper dimples observed on the fracture surfaces of the FSW + LSP specimens (Figure 12d–f) are consistent with more extensive local plastic deformation before fracture than in the untreated specimens (Figure 12a–c).

The larger, deeper dimples in the LSP-treated specimens are consistent with more extensive local plastic deformation before fracture and complement the higher elongation measured in the tensile tests. Fracture-surface observations alone cannot establish whether LSP delayed the onset of necking or crack initiation.

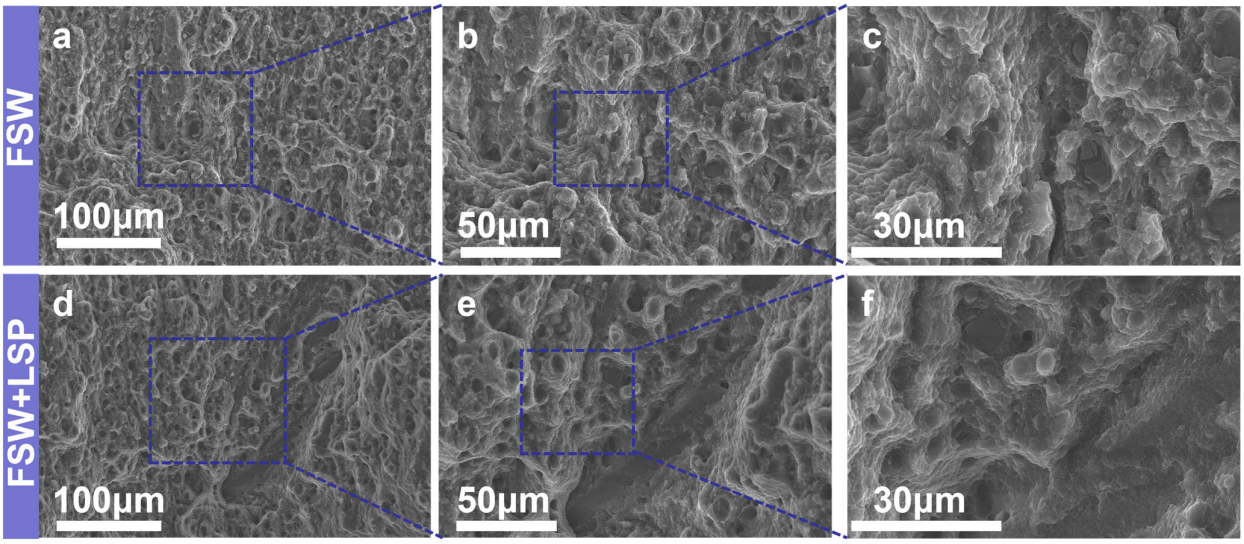


Figure 12. Microscopic morphologies of fracture planes. (**a–c**) FSW joint; (**d–f**) FSW + LSP joint. The dotted line and frame indicate an enlarged view of the selected region.

4. Discussion

4.1. Depth-Dependent Microstructural Modification

In the untreated 7075 FSW joint, the mean grain sizes at depths of 100, 500 and 900 μm below the top surface were 7.95, 8.16 and 8.19 μm, respectively (Figure 4a–c). He et al. [35] reported a larger grain-size difference across an AA7075 weld nugget, with mean values of approximately 6 μm near the top and 3.5 μm near the bottom. Their measurements spanned the upper and lower regions of the nugget, whereas the three regions examined here were all within 0.9 mm of the top surface of a 4 mm thick joint. The small variation observed here therefore characterises the sampled near-surface region. Comparing the treated and untreated joints at corresponding depths, the largest refinement occurred at 100 μm, where LSP reduced the mean grain size from 7.95 to 1.54 μm. The difference between the two joints diminished with depth.

Figures 5 and 6 describe complementary features of the final microstructure. The grain classification map and the KAM map describe different features of the final microstructure. In S1, the fraction classified as recrystallised increased from 80.9% to 85.2% after LSP, while the mean KAM decreased from 0.63° to 0.38°. A finer grain structure can be accompanied by lower local orientation differences between the neighbouring points included in the KAM calculation. These observations do not independently establish whether dynamic recrystallisation occurred during LSP. Following LSP, the mean KAM

decreased from 0.63° to 0.38° in S1 and from 0.78° to 0.68° in S2, while the values in S3 were similar before and after treatment. Thus, the largest measured change occurred in the near-surface region. The decrease in S1 accompanied substantial grain refinement, from 7.95 to 1.54 μm. Grain subdivision and dislocation rearrangement may both affect local orientation gradients, while the calculated KAM also depends on the treatment of neighbouring misorientations at grain boundaries. The present measurements do not separate these effects. Therefore, the change in KAM can be compared between depths, but the relative contributions of the individual factors cannot be ranked.

4.2. Residual Stress Redistribution and Local Hardening

LSP changes the near-surface residual stress from tensile to compressive, with a surface value of approximately −280 MPa. This redistribution is consistent with nonuniform plastic deformation under shock loading followed by elastic constraint during unloading. The plastically deformed surface region is constrained by the surrounding and underlying material, allowing compressive residual stresses to remain after the shock load is removed. With increasing depth, the shock-induced deformation becomes less pronounced, and the residual stress gradually approaches the distribution of the untreated joint.

After LSP with an ablative tape and water confinement, the residual stress parallel to the weld was approximately −280 MPa at the treated surface of the 7075 joint. Sanchez et al. [26] reported a surface residual stress of approximately −330 MPa from XRD measurements on laser-peened AA7075-T651 plate treated with an ablative coating. Their hole-drilling measurements placed the maximum compression below the surface, where both the longitudinal and transverse plate stresses reached approximately −400 MPa. The depth profiles also differed. In the present joint, the weld-longitudinal stress changed from compression to tension at 0.5–0.6 mm, whereas Sanchez et al. still measured compression at 1 mm. In the present measurements, 0.9 mm marks the depth at which the treated and untreated profiles approached each other. The initial weld stress state, the measurement direction and the depth-profiling method all affect how these results can be compared.

The near-surface hardness increase is broadly consistent with the observed grain refinement. At a depth of 0.5 mm, the hardness increases from 126.8 to 135.6 HV, indicating greater resistance to local indentation deformation. Nevertheless, hardness depends on several interacting factors, including grain size, dislocation structure, precipitation state, and residual stress. Consequently, the hardness results support local strengthening but do not independently quantify the contribution of each mechanism.

4.3. Relationship Between Surface Modification and Tensile Performance

At a depth of 100 μm in the nugget zone, the mean grain size was 7.95 μm in the untreated joint and 1.54 μm after LSP. According to the Hall–Petch relationship, a smaller grain size is expected to increase the local yield stress by impeding dislocation slip at grain boundaries. The increase in hardness from 126.8 to 135.6 HV at a depth of 0.5 mm provides separate evidence of subsurface hardening. During transverse tensile loading, the modified surface layer and the underlying material carry load together. Because grain refinement diminished with depth in the 4-mm-thick joint, the near-surface grain size alone cannot predict the section-averaged tensile response. Local hardening may nevertheless have contributed to the measured increases in joint yield strength from 346.8 to 383.9 MPa and ultimate tensile strength from 381.2 to 419.8 MPa.

The surface residual stress measured parallel to the weld was approximately −280 MPa after LSP. This stress component changed from compression to tension at a depth of 0.5–0.6 mm, corresponding to 12.5–15% of the specimen thickness. This percentage de-

scribes the depth of longitudinal compression. The grain-size measurements at S1–S3 provide a separate measure of how refinement varied with depth. Because the tensile loading axis was perpendicular to the weld, the measured residual stress acted transverse to the applied load. It may have influenced local yielding through the multiaxial stress state. Its contribution to the joint tensile response remains uncertain because the loading-direction residual stress and its evolution during plastic deformation were not measured.

Mean elongation after fracture increased from 5.47 ± 0.23% to 7.13 ± 0.27% (mean ± SD, n = 3 per condition). The absolute gain was 1.66 percentage points, corresponding to a relative increase of approximately 30.3% from the untreated value. Elongation after fracture reflects the plastic strain accumulated over the gauge length, including deformation localised near the fracture. The Hall–Petch relationship therefore does not provide a direct prediction of this quantity. One possible explanation is that the depth-dependent variation in local strength altered the distribution of plastic strain during loading. Establishing whether this redistribution delayed strain localisation would require spatially resolved strain measurements across the weld.

Dai et al. [30] attributed the elongation gain in their joints to more uniform properties across the weld and reduced strain localisation. Our measurements resolve a different aspect of the joint response: the extent of grain refinement varied with depth beneath the treated surface. Wu et al. [36] showed that interaction between layers can influence strain hardening in gradient-structured steel. A similar interaction is a possible explanation for the tensile response observed here, although its contribution would require local strain measurements to establish. The present results link depth-resolved grain refinement and residual stress redistribution with local hardening and improved transverse tensile properties in the same 7075 joint condition.

5. Conclusions

This study examined how laser shock peening of the top surface of friction-stir-welded 7075 aluminium alloy joints affected the nugget-zone microstructure, residual stress distribution, and tensile response of the 4-mm-thick joints. The main findings can be summarized as follows:

(1) LSP reduced the near-surface mean grain size in the nugget zone from 7.95 to 1.54 μm. With increasing depth, the mean grain size in the FSW + LSP joint approached that of the untreated FSW joint. At a depth of 0.5 mm, hardness increased from 126.8 to 135.6 HV. These measurements show that grain refinement was strongest near the treated surface and that local hardening extended into the subsurface.

(2) LSP changed the longitudinal residual stress at the treated surface from tensile to compressive, with a surface value of approximately −280 MPa. The compressive layer extended to a depth of 0.5–0.6 mm. The difference between the FSW and FSW + LSP stress profiles continued to diminish below this layer, and the profiles approached each other at approximately 0.9 mm.

(3) Relative to the untreated FSW joints, the FSW + LSP joints exhibited increases in mean yield strength from 346.8 to 383.9 MPa, ultimate tensile strength from 381.2 to 419.8 MPa, and elongation after fracture from 5.47% to 7.13%. Thus, one-sided LSP produced gains of approximately 10% in both strength measures and 1.66 percentage points in elongation. These joint-level gains accompanied a depth-dependent surface modification. The measurements establish local hardening, while the individual contributions of grain refinement and residual stress redistribution to the tensile response remain unresolved.

Author Contributions: Conceptualization, B.H.; methodology, B.H.; investigation, B.H.; formal analysis, B.H.; data curation, B.H.; visualization, B.H.; writing—original draft preparation, B.H.;

writing—review and editing, B.H. and L.L.; supervision, L.L. All authors have read and agreed to the published version of the manuscript.

Funding: This research was jointly funded by the Quality Engineering Project of Chuzhou Polytechnic (Grant No. 2025jnds02) and the Anhui Provincial Department of Education Talent Program (Grant No. JNFX2026136).

Data Availability Statement: The original contributions presented in this study are included in the article. Further inquiries can be directed to the corresponding author.

Conflicts of Interest: The authors declare no conflicts of interest. The funders had no role in the design of the study; in the collection, analyses, or interpretation of data; in the writing of the manuscript; or in the decision to publish the results.

References

1. Dursun, T.; Soutis, C. Recent developments in advanced aircraft aluminium alloys. *Mater. Des.* **2014**, *56*, 862–871. https://doi.org/10.1016/j.matdes.2013.12.002.
2. Zheng, J.; Pang, Q.; Hu, Z.; Sun, Q. Recent progress on regulating strategies for the strengthening and toughening of high-strength aluminum alloys. *Materials* **2022**, *15*, 4725. https://doi.org/10.3390/ma15134725.
3. Uematsu, Y.; Tokaji, K.; Tozaki, Y.; Shibata, H. Fatigue behaviour of friction stir welded A7075-T6 aluminium alloy in air and 3% NaCl solution. *Q. J. Jpn. Weld. Soc.* **2009**, *27*, 261–269. https://doi.org/10.2207/qjjws.27.261.
4. Holzer, M.; Hofmann, K.; Mann, V.; Hugger, F.; Roth, S.; Schmidt, M. Change of hot cracking susceptibility in welding of high strength aluminum alloy AA 7075. *Phys. Procedia* **2016**, *83*, 463–471. https://doi.org/10.1016/j.phpro.2016.08.048.
5. Sokoluk, M.; Cao, C.; Pan, S.; Li, X. Nanoparticle-enabled phase control for arc welding of unweldable aluminum alloy 7075. *Nat. Commun.* **2019**, *10*, 98. https://doi.org/10.1038/s41467-018-07989-y.
6. Kosturek, R.; Torzewski, J.; Wachowski, M.; Śnieżek, L. Effect of welding parameters on mechanical properties and microstructure of friction stir welded AA7075-T651 aluminium alloy butt joints. *Materials* **2022**, *15*, 5950. https://doi.org/10.3390/ma15175950.
7. Akbari, M.; DebRoy, T.; Asadi, P.; Sadowski, T. Recent advances in friction stir welding/processing tools. *J. Manuf. Process.* **2025**, *142*, 99–156. https://doi.org/10.1016/j.jmapro.2025.03.089.
8. El-Zathry, N.E.; Akinlabi, S.; Woo, W.L.; Patel, V.; Mahamood, R.M. Friction Stir-Based Techniques: An Overview. *Weld. World* **2025**, *69*, 327–361. https://doi.org/10.1007/s40194-024-01847-w.
9. Rajakumar, S.; Muralidharan, C.; Balasubramanian, V. Influence of friction stir welding process and tool parameters on strength properties of AA7075-T6 aluminium alloy joints. *Mater. Des.* **2011**, *32*, 535–549. https://doi.org/10.1016/j.matdes.2010.08.025.
10. Mahoney, M.W.; Rhodes, C.G.; Flintoff, J.G.; Bingel, W.H.; Spurling, R.A. Properties of friction-stir-welded 7075 T651 aluminum. *Metall. Mater. Trans. A* **1998**, *29*, 1955–1964. https://doi.org/10.1007/s11661-998-0021-5.
11. Padhy, G.K.; Wu, C.S.; Gao, S. Auxiliary energy assisted friction stir welding—Status review. Sci. Technol. *Weld. Join.* **2015**, *20*, 631–649. https://doi.org/10.1179/1362171815Y.0000000048.
12. Bagheri, B.; Abbasi, M.; Dadaei, M. Mechanical behavior and microstructure of AA6061-T6 joints made by friction stir vibration welding. *J. Mater. Eng. Perform.* **2020**, *29*, 1165–1175. https://doi.org/10.1007/s11665-020-04639-7.
13. Bagheri, B.; Abbasi, M. Analysis of microstructure and mechanical properties of friction stir vibration welded (FSVW) 5083 aluminum alloy joints: Experimental and simulation. *J. Weld. Join.* **2019**, *37*, 243–253. https://doi.org/10.5781/JWJ.2019.37.3.8.
14. Bagheri, B.; Abbasi, M.; Givi, M. Effects of vibration on microstructure and thermal properties of friction stir spot welded (FSSW) aluminum alloy (Al5083). *Int. J. Precis. Eng. Manuf.* **2019**, *20*, 1219–1227. https://doi.org/10.1007/s12541-019-00134-9.
15. Bagheri, B.; Abbasi, M.; Abdollahzadeh, A. Microstructure and mechanical characteristics of AA6061-T6 joints produced by friction stir welding, friction stir vibration welding and tungsten inert gas welding: A comparative study. *Int. J. Miner. Metall. Mater.* **2021**, *28*, 450–461. https://doi.org/10.1007/s12613-020-2085-1.
16. Bagheri, B.; Abbasi, M.; Dadaei, M. Effect of water cooling and vibration on the performances of friction-stir-welded AA5083 aluminum joints. *Metallogr. Microstruct. Anal.* **2020**, *9*, 33–46. https://doi.org/10.1007/s13632-019-00606-4.
17. Baradarani, F.; Emami, S.; Mostafapour, A.; Khan, M.D.F. Influence of ultrasonic vibration on the microstructure and texture evolution of AZ91 magnesium alloy during ultrasonic-assisted friction stir welding. *Weld. World* **2021**, *65*, 2371–2382. https://doi.org/10.1007/s40194-021-01157-5.

18. Wang, K.; Naumov, A.; Panchenko, E.; Panchenko, O. A Review on Friction Stir Welding of High-Strength Al-Zn-Mg Alloy: Insights on Second-Phase Particles. *Materials* **2024**, *17*, 5107. https://doi.org/10.3390/ma17205107.
19. Lezaack, M.B.; Simar, A. Avoiding abnormal grain growth in thick 7XXX aluminium alloy friction stir welds during T6 post heat treatments. *Mater. Sci. Eng. A* **2021**, *807*, 140901. https://doi.org/10.1016/j.msea.2021.140901.
20. Ding, K.; Ye, L. *Laser Shock Peening: Performance and Process Simulation*; Woodhead Publishing: Cambridge, UK, 2006. https://doi.org/10.1533/9781845691097.
21. Montross, C.S.; Wei, T.; Ye, L.; Clark, G.; Mai, Y.W. Laser shock processing and its effects on microstructure and properties of metal alloys: A review. *Int. J. Fatigue* **2002**, *24*, 1021–1036. https://doi.org/10.1016/S0142-1123(02)00022-1.
22. Pan, X.; Zhou, L.; Wang, C.; Yu, K.; Zhu, Y.; Yi, M.; Wang, L.; Wen, S.; He, W.; Liang, X. Microstructure and residual stress modulation of 7075 aluminum alloy for improving fatigue performance by laser shock peening. *Int. J. Mach. Tools Manuf.* **2023**, *184*, 103979. https://doi.org/10.1016/j.ijmachtools.2022.103979.
23. Dhakal, B.; Swaroop, S. Mechanical properties and deformation dependent microstructural aspects of laser shock peened 7075-T6 aluminum alloy without coating. *Mater. Charact.* **2022**, *183*, 111620. https://doi.org/10.1016/j.matchar.2021.111620.
24. He, Z.; Shen, Y.; Tao, J.; Chen, H.; Zeng, X.; Huang, X.; Abd El-Aty, A. Laser shock peening regulating aluminum alloy surface residual stresses for enhancing the mechanical properties: Roles of shock number and energy. *Surf. Coat. Technol.* **2021**, *421*, 127481. https://doi.org/10.1016/j.surfcoat.2021.127481.
25. Kumar, H.; Kaufman, J.; Pathak, S.; Kopeček, J.; Šmaus, J.; Gadalińska, E.; Stránský, O.; Čáp, F.; Brajer, J. Laser power density driven residual stress and surface quality of AA7075 alloy under laser shock peening. *Int. J. Adv. Manuf. Technol.* **2026**. https://doi.org/10.1007/s00170-026-19055-9.
26. Sanchez, A.G.; Leering, M.; Glaser, D.; Furfari, D.; Fitzpatrick, M.E.; Wharton, J.A.; Reed, P.A.S. Effects of ablative and non-ablative laser shock peening on AA7075-T651 corrosion and fatigue performance. *Mater. Sci. Technol.* **2021**, *37*, 1015–1034. https://doi.org/10.1080/02670836.2021.1972272.
27. Palmeh, R.; Pour-Ali, S.; Tavangar, R.; Khan, M.F. Correlation between the micro-shot peening coverage and surface microstructural evolution and fluoride-induced corrosion behavior in Monel 400 alloy. *Mater. Today Commun.* **2024**, *39*, 108625. https://doi.org/10.1016/j.mtcomm.2024.108625.
28. Dhanasekaran, M.P.; Agilan, M.; Avinash, S.; Vidyananda, K.N.; Rao, G.S.; Mahapatra, D.R. Influence of laser shock peening on residual stress and microhardness of AA2219 friction stir weld. *Mater. Lett.* **2024**, *356*, 135586. https://doi.org/10.1016/j.matlet.2023.135586.
29. Li, K.; He, X.; Li, L.; Yang, L.; Hu, J. Residual stress distribution of aluminium-lithium alloy in hybrid process of friction stir welding and laser peening. *Opt. Laser Technol.* **2022**, *152*, 108149. https://doi.org/10.1016/j.optlastec.2022.108149.
30. Dai, W.; Guo, W.; Li, Q.; Xiao, J.; Li, W.; Zhang, H. Homogenization of local microstructure and mechanical properties in friction stir welded Al-Cu alloy joint achieved through laser shock peening. *J. Mater. Process. Technol.* **2024**, *333*, 118579. https://doi.org/10.1016/j.jmatprotec.2024.118579.
31. Wu, C.; Chen, L.; Li, J.; Meng, X.; Guo, L.; Feng, X. Laser shock peening of 6061-T6 aluminum alloy friction stir welding joints: Microstructure evolution, fracture morphology and strengthening mechanism. *J. Mater. Res. Technol.* **2025**, *39*, 3981–3998. https://doi.org/10.1016/j.jmrt.2025.10.103.
32. Dhanasekaran, M.P.; Agilan, M.; Jalaja, K.; Prabhu, T.A.; Muthukumar, R.; Mahapatra, D.R. Impact of laser shock peening on microstructure and cryogenic tensile behaviour of AA2219 friction stir weld. *J. Manuf. Process.* **2026**, *173*, 302–314. https://doi.org/10.1016/j.jmapro.2026.06.074.
33. Hatamleh, O.; Lyons, J.; Forman, R. Laser and shot peening effects on fatigue crack growth in friction stir welded 7075-T7351 aluminum alloy joints. *Int. J. Fatigue* **2007**, *29*, 421–434. https://doi.org/10.1016/j.ijfatigue.2006.05.007.
34. Hatamleh, O.; DeWald, A. An investigation of the peening effects on the residual stresses in friction stir welded 2195 and 7075 aluminum alloy joints. *J. Mater. Process. Technol.* **2009**, *209*, 4822–4829. https://doi.org/10.1016/j.jmatprotec.2008.12.010.
35. He, C.; Kitamura, K.; Yang, K.; Liu, Y.-J.; Wang, Q.-Y.; Chen, Q. Very high cycle fatigue crack initiation mechanism in nugget zone of AA 7075 friction stir welded joint. *Adv. Mater. Sci. Eng.* **2017**, *2017*, 7189369. https://doi.org/10.1155/2017/7189369.
36. Wu, X.; Jiang, P.; Chen, L.; Yuan, F.; Zhu, Y.T. Extraordinary strain hardening by gradient structure. *Proc. Natl. Acad. Sci. USA* **2014**, *111*, 7197–7201. https://doi.org/10.1073/pnas.1324069111.

Disclaimer/Publisher's Note: The statements, opinions and data contained in all publications are solely those of the individual author(s) and contributor(s) and not of MDPI and/or the editor(s). MDPI and/or the editor(s) disclaim responsibility for any injury to people or property resulting from any ideas, methods, instructions or products referred to in the content.